Surface & Coatings Technology 349 (2018) 24–31

Contents lists available at ScienceDirect

Surface & Coatings Technology

journal homepage: www.elsevier.com/locate/surfcoat

Stability of nano-hydroxyapatite thin coatings at liquid/solid interface

Nimshi L. Fernando[a], Nilwala Kottegoda[b,c], Sumedha Jayanetti[a], Veranja Karunaratne[c,d], Dilushan R. Jayasundara[a,*]

[a] Department of Physics, University of Colombo, Colombo 03, Sri Lanka
[b] Center for Advanced Materials Research/Department of Chemistry, Faculty of Applied Sciences, University of Sri Jayewardenepura, Gangodawila, Nugegoda, Sri Lanka
[c] Sri Lanka Institute of Nanotechnology, Mahenwatta, Pitipana, Sri Lanka
[d] Department of Chemistry, University of Peradeniya, Peradeniya, Sri Lanka

ARTICLE INFO

Keywords:
Nano-hydroxyapatite
Thin coatings
Gold
Quartz crystal microbalance
Liquid/solid interface
Stability

ABSTRACT

The stability of nano-hydroxyapatite thin coatings immediately after deposition, sonication and prolong water exposure was monitored using the quartz crystal microbalance. Different morphological forms of nano-hydroxyapatite particles were obtained using three different synthesis routes. Electrophoretic deposition and spin coating techniques were used for the fabrication of nano-hydroxyapatite coatings on gold quartz crystal microbalance sensors. Synthesized nano-hydroxyapatite particles and coatings were characterized by spectroscopic techniques such as, Powder X-ray Diffraction (PXRD) and Fourier Transform Infrared (FTIR), and Scanning Electron Microscopy (SEM). All resulting thin coatings showed stability under ultrasonic treatment in aqueous medium, however the stability varied under subsequent prolong exposure to similar mediums. Comparative studies on these thin coatings indicated that the resulting coating morphology in the form of preferential crystal orientation, and the solution at interface are the key parameters that control the thin coating stability.

1. Introduction

In recent times functional coatings have increasingly become popular in the design and development of smart surfaces. These include multiple tasks such as protection from corrosion and fouling to environmental sensing. It has also become an economical and a practical method for overcoming compatibility issues at interfaces. Functional coatings, specifically in the areas related to bio medical applications are generally fabricated on surfaces such as gold, due to its bio compatibility, non-toxicity and non-corrosive properties [1].

Hydroxyapatite (HA) and its nano-derivatives have been exploited in medical applications, such as coatings on metal implants [2], dental [3], drug delivery [4,5] and agricultural applications [6,7]. It is the main mineral component of bone and shows excellent biocompatibility, slow bio degradability, sustained drug release properties, osteoconductivity and mechanical properties. Increasingly HA coatings are now being considered for applications in biosensing [8,9].

Fabrication of HA on metallic substrates can be achieved by; plasma sputtering [10], pulse laser deposition [11], sol-gel coating [12], electrophoretic deposition (EPD) [13–18] and spin coating techniques [19,20]. However all of these techniques require high temperature annealing to obtain a stable homogeneous coating. Out of the above methods, EPD is one of the most scalable and cost effective methods to develop HA thin coatings on solid surfaces. The EPD method involves the migration and later deposition of charged particles under the influence of an electric field. Sintering at a very high temperature is needed for better adherence of HA on to metal substrates after deposition. However, in applications such as biosensors, high temperature treatment is not an option where it would cause degradation of the HA coating and deterioration of the metal substrates [21]. Monokawa et al. have fabricated homogeneous nano-thin layer of HA nanoparticles (HA-Np) on the gold surface using EPD without sintering the coating at high temperatures [22]. HA biosensors were developed in order to sense proteins such as feral bovine serum [23] and fibrinogen [9] in the phosphate buffer solution (PBS) medium.

Spin coating is another predominant technique used to produce uniform thin coatings with the thickness of the order of micrometers and nanometers [19]. Zhengpeng et al. have developed a HA biosensor using the spin coating technique to study the adsorption/desorption behaviors of the bovin serum albumin in water [8] on gold and titanium surfaces.

In situ stability of coatings in most aqueous mediums, especially of those coatings used in biosensing applications, is essential for their accurate performance. However, in most studies the dissolution resistance of HA-Np coatings and the interactions of HA-Np with aqueous media over an extended period of time were not investigated

* Corresponding author.
E-mail address: dilushanj@phys.cmb.ac.lk (D.R. Jayasundara).

https://doi.org/10.1016/j.surfcoat.2018.05.042
Received 25 February 2018; Received in revised form 9 May 2018; Accepted 22 May 2018
Available online 23 May 2018
0257-8972/

adequately. Quartz crystal microbalance (QCM) is an in situ technique that can be used to measure molecular adsorption and desorption at an interface with nano gram resolution [24–28]. In the present study, using QCM we report that HA-Np coatings prepared via EPD and spin coating techniques, under ambient conditions show stability under ultrasonic treatment in aqueous medium. However it is observed that this stability varies under subsequent prolong exposure to similar mediums. The observed variation in the thin HA-Np coating stability during the prolong exposure can be related to the preferential crystal orientation of the HA-Np on the gold surface. Further, we also observe that the dissolution of HA-Np coatings are influenced by the type of aqueous medium used. Thus, it indicates that the resulting film morphology and the solution at interface are the key parameters that control the coating stability.

2. Materials & methods

2.1. Chemicals and materials

Calcium hydroxide ($Ca(OH)_2$) (95% Sigma), ortho-phosphoric acid (H_3PO_4) (88%, Sigma), absolute ethanol (C_2H_5OH) (99%, VWR chemicals), hydrogen peroxide(H_2O_2) (35 wt%, Sigma), sulfuric acid (H_2SO_4) (97%, Sigma), diammonium hydrogen phosphate ($(NH_4)_2HPO_4$) (98%, Sigma), calcium acetate ($Ca(CH_3COO)_2$) (99%, Sigma), potassium dihydrogen phosphate (KH_2PO_4) (99%, Sigma) and potassium hydrogen phosphate (K_2HPO_4) (98%, Sigma) were used as received. Deionized water was used for all aqueous solutions. All glassware, reactions cell and Au QCM crystals were cleaned with piranha solution (3:1, H_2SO_4 to H_2O_2) prior to use.

2.2. Synthesis of HA-Np

Synthesis of HA-Np was carried out using three different methods and are referred to as Route 1, Route 2 and Route 3. These routes have been reported to give different morphologies of HA-Np.

2.2.1. Route 1

HA-Np were synthesized by a wet chemical method as described by Mateus et al. [29] (HA-Np (R1)). In summary, aqueous solutions of Ca $(OH)_2$ and H_3PO_4 were used where the Ca: P molar ratio was 1.67. In the synthesis, 0.6 M H_3PO_4 was added drop-wise into a suspension of 1.0 M Ca $(OH)_2$, while stirring vigorously under mechanical agitation (1000 rpm). The synthesis can be described by the following chemical equation.

$$6\ H_3PO_4 + 10\ Ca(OH)_2 \rightarrow Ca_{10}(PO_4)_6(OH)_2 + 18\ H_2O$$

2.2.2. Route 2

HA-Np were synthesized as described by Santos et al. [30] (HA-Np (R2)). A suspension of 0.3 M $(NH_4)_2HPO_4$ was added drop wise into a 0.5 M $Ca(OH)_2$ suspension to obtain Ca: P molar ratio of 1.67. The reaction was carried out at 40 °C for approximately one hour, while stirring vigorously under mechanical agitation (1000 rpm). The solution was then allowed to cool to room temperature. The reaction is described by the following chemical formulae.

$$10\ Ca(OH)_2 + 6\ (NH_4)_2{\cdot}HPO_4 \rightarrow Ca_{10}(PO_4)_6(OH)_2 + 18H_2O + 12NH_3$$

2.2.3. Route 3

HA-Np were synthesized as described by Wei et al. [31] (HA-Np (R3)). Initially, 2.20 g of $Ca(CH_3COO)_2$ was dissolved in 300 ml de-ionized water, where the pH of the initial solution was 8.2. Subsequently the pH value of the solution was adjusted to 11, by adding strong ammonia. Then, 190 ml of de-ionized water was added to the above solution. While vigorously stirring with a magnetic stirrer, 126 ml of 0.6 M $(NH_4)_2HPO_4$ solution was added dropwise into the $Ca(CH_3COO)_2$ solution at a rate of 10 ml/min through a funnel containing a filter paper. The mixed solution was then heated to 40 °C and kept for 3 h under continuous stirring. The solution was then allowed to cool to room temperature. The synthesis can be described by the following chemical equation.

$$10\ Ca(CH_3COO)_2 + 6\ (NH_4)_2HPO_4 + 8\ NH_3OH \rightarrow Ca_{10}(PO_4)_6(OH)_2 + 20CH_3COONH_4 + 2\ H_2O$$

HA-Np synthesized by all 3 routes were allowed to settle and the supernatant was decanted. Deionized water was used to wash the resulting HA-Np and was dried at 80 °C for 2 h. All samples were kept in a desiccator prior to use.

2.3. Characterization

Powder X-ray diffraction (PXRD) patterns of all synthesized samples were recorded using a Bruker D8 Focus X-ray powder diffractometer using CuK α radiation (λ = 0.154 nm) over a 2θ range of 3–60°, with a step size of 0.02° and a step time of 1 s. The crystallite size was estimated from the full width at half maximum (FWHM) according to Scherer's equation [9,32–34].

The chemical nature and molecular bonding of the HA-Np samples were studied using Fourier Transform Infrared (FTIR) Spectrometer (Thermo Scientific Nicolet IS 10) under ATR mode. IR spectra were recorded between 4000 and 600 cm^{-1} with a wavenumber resolution of 0.5 cm^{-1}.

The particle size and morphology of the synthesized samples were studied using a scanning electron microscopy (SEM) (Zeiss evo ls 15, EHT 20 KV, Mag: 60KX). HA-Np were deposited on Au QCMs using identical conditions for comparison. Samples were coated with a thin gold coating prior to imaging. The size distribution of the HA-Np observed in the SEM was measured using the ImageJ software, where the sample areas were carefully selected away from the clusters.

2.4. Monitoring the dissolution resistance

Crystals of 10 MHz fundamental resonance frequency with 100 nm thick vapor-deposited gold electrodes (International Crystal Manufacturing) were used as the substrate in this study. The surface of the QCM was cleaned with piranha solution and washed with copious amounts of de ionized water before fabrication of HA-Np [35].

HA-Np powder was ultra-sonically dispersed in absolute ethanol for 1 h to form a HA-Np suspension. The prepared suspension was used to fabricate HA-Np on gold QCMs using spin coating and EPD techniques. Spin coating was done at 3500 rpm for 5 min [8]. A thin layer of HA-Np was deposited by EDP method using the QCM as the cathode, 316 l stainless steel as the anode and HA-Np in Et-OH suspension as the electrolyte [9]. Similar amounts of HA-Np coatings were fabricated on gold by varying the time during EPD at a constant voltage of 10 *V*. The ultrasonic treatment (28 kHz, 100 W) for 5 s in deionized water was given to remove the loosely bound HA-Np from the deposited layer on the cathode. The coatings were finally heat-treated under a tungsten lamp for 3 h in order to consolidate the HA-Np and gold surface.

The QCM setup consists of a Gamry eQCM 10 M and a static Teflon reaction cell (International Crystal Manufacturing) connected to a computer for data recording using Gamry resonator software. Change in the resonance frequency of the QCM before and after fabrication of the coating was monitored. The amount deposited on the QCMs was calculated from the measured change in frequency using Sauerbrey equation.

HA-Np coated QCMs were then sonicated in deionized water for 5 s repetitively, until the change in resonance frequency became constant. Once stable, the change in the resonance frequency before and after sonication was recorded.

The stability of the thin HA-Np coatings after 20 h, which is referred to as prolong exposure, in water was monitored. For this the HA-Np

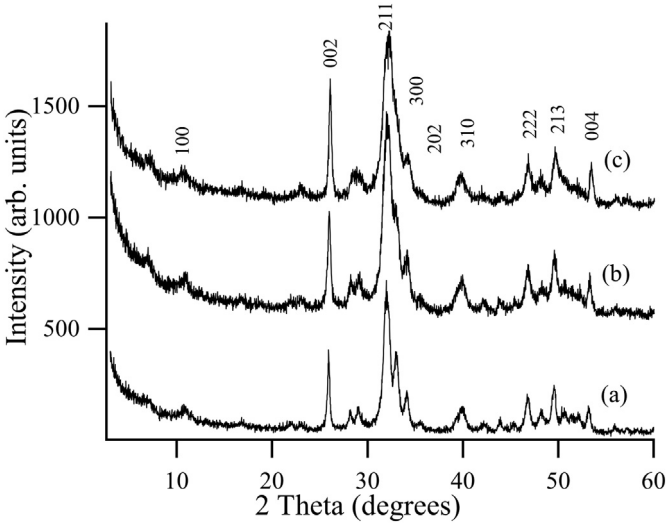

Fig. 1. PXRD patterns of synthesized HA-Np; (a) HA-Np (R1), (b) HA-Np (R2), (c) HA-Np (R3).

coated QCM was clamped in the Teflon static cell, where only the coated surface being exposed to the aqueous medium. Deionized water was introduced into the cell and the HA-Np coated QCM was exposed to water for 20 h. The solution was then decanted and the QCM was dried. The change in the resonance frequency of the dry QCM before and after exposure to water was obtained.

Above procedure was repeated with a 10 mM phosphate buffer solution (PBS), for both spin coated and EPD coated QCMs, as biological reactions are conducted in PBS solution (KH_2PO_4 and K_2HPO_4, pH 7.0).

3. Results & discussion

3.1. Powder X-ray diffraction

PXRD patterns of the synthesized HA-Np using the three different routes are shown in Fig. 1. The patterns are similar and in agreement with previously reported PXRD data on HA-Np that show diffraction from (100), (002), (211), (300), (202), (310), (222), (213) and (004) planes [6]. It also indicates a single phase without traces of other crystalline phases such as calcium hydroxide, tri calcium phosphate and calcium carbonate.

The diffraction peaks from (002) and (100) planes reflect the crystallinity perpendicular to these planes and correspond to *c* and *a* crystal directions which defines the crystallinity of HA-Np [9,36,37]. The crystallite sizes along these directions can be calculated using FWHM and Scherrer's equation [37],

$$B = \frac{K\,\lambda}{L\,\cos\theta}$$

where, peak width is given by *B*, crystallite size is given by *L*, a dimensionless shape factor is given by *K* (*K* = 0.9), X-ray wavelength is given by λ and the Bragg angle (in degrees) is given by *θ*. These data are presented in Table 1, along with the intensity ratio of I_{002}/I_{100}.

The data show larger crystallite size perpendicular to the (002) plane compared to that of (100) plane for HA-Np synthesized from all three routes. These results are in line with reports that describe HA-Np crystal growth occur predominantly along the c-axis, making diffraction from (002) plane to be the dominant peak in PXRD spectra [7]. It can also be observed from Table 1 that the crystallite sizes and I_{002}/I_{100} ratio of HA-Np (R2) in both *c* and *a* directions are smaller than that of HA-Np crystals synthesized via other two routes, indicating lower crystallinity in HA-Np (R2) compared with the other two HA-Np types.

Table 1
The crystal sizes perpendicular to (100) & (002) planes and peak heights in the form of $I_{(002)}/I_{(100)}$ ratio.

	HA-Np (R1)	HA-Np (R2)	HA-Np (R3)
Crystal sizes perpendicular to (100) plane	8.9 nm	6.8 nm	11.9 nm
Crystal sizes perpendicular to (002) plane	28.7 nm	21.8 nm	28.5 nm
$I_{(002)}/I_{(100)}$	9.5	6.6	17.6

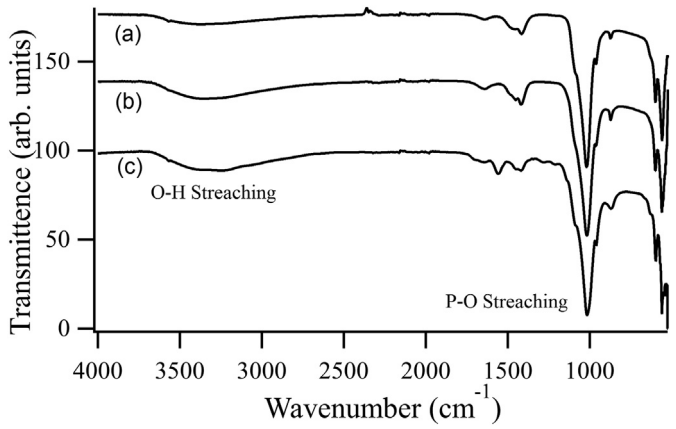

Fig. 2. FTIR spectra of synthesized HA-Np; (a) HA-Np (R1), (b) HA-Np (R2), (c) HA-Np (R3).

3.2. Infrared spectroscopy

FTIR spectra of the synthesized HA-Np are shown in Fig. 2. The most prominent sharp and intense absorption band located around 1085 cm^{-1} represents the symmetric P—O stretching vibrations of PO_4^{-3} ions in HA. The Broad absorption band centered at 3500 cm^{-1} is attributed to the O—H stretching of the hydroxyl groups. Further, minor peaks around 1400 cm^{-1} are attributed to O—H—O bending of water molecules [38]. These observations are consistent with the IR absorbance reported earlier on HA-Np. [6,7]

3.3. Scanning electron microscopy

SEM analysis was carried out in order to further understand the morphology of the synthesized HA-Np. Fig. 3 shows the SEM images of spin coated HA-Np onto Au QCMs from the three different synthesis routes. These images show the morphological differences in the HA-Np prepared by the three routes. In the SEM of HA-Np (R1), shown in Fig. 3(a), rod-like particles can be observed distributed inhomogeneously on the QCM surface. Further it can be observed that some of these nano particles have formed clusters on the surface during deposition. However, in the SEM image (Fig. 3(b)) of HA-Np (R2) show a much dense and homogeneous distribution of smaller particles. Much more clustered and inhomogeneously distributed particles can be observed in the SEM image of HA-Np (R3) as shown in Fig. 3(c).

Quantitative analysis of the size distribution of the HA-Np observed in the SEM for HA-Np (R1) and HA-Np (R2) were carried out over equivalent sample areas away from cluster sites and their size distribution is shown in Fig. 4. The size distribution of the HA-Np (R3) was not carried out as the particles are highly clustered and could not be resolved even in the high resolution image of HA-Np (R3) (see supplementary information Fig. S1). The above analysis show a significant difference in the length distribution for HA-Np (R1) and HA-Np (R2), where length of the HA-Np (R2) (Fig. 4(b)) has a smaller particle size compared to that of HA-Np (R1) (Fig. 4(a)). Further it can also be observed that the nanoparticle length distribution is wider for HA-Np (R2)

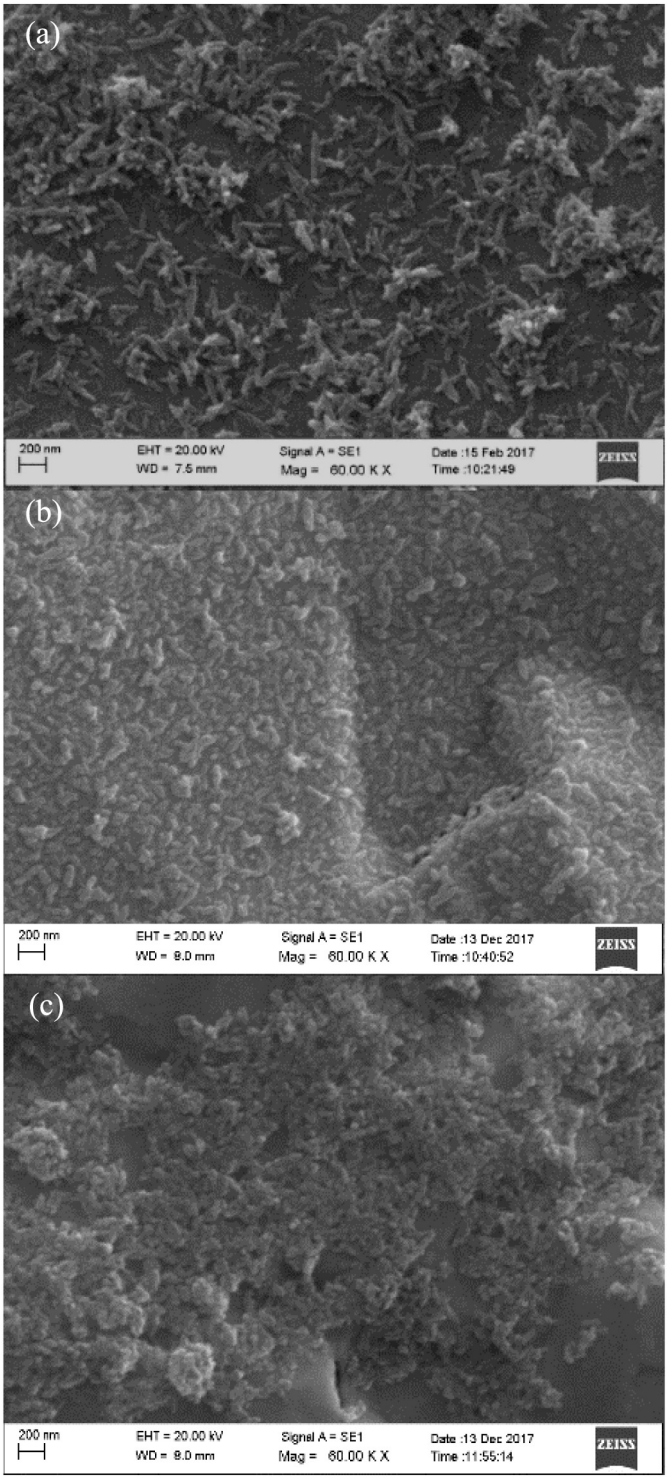

Fig. 3. SEM images of synthesized HA-Np spin coated on Au QCMs; (a) HA-Np (R1), (b) HA-Np (R2), (c) HA-Np (R3). The SEM images were taken at a magnification of 60 K X with scale bar representing 200 nm.

compared to that of HA-Np (R1). The width distribution of the HA-Np calculated from the SEM images (Fig. 3 (a) and (b)) was in the range 30–55 nm and is consistent with the reported data [7].

It is reported that the growth of the HA-Np nanorods occurs along the *c* axis (perpendicular to (002) plane) where bead like particles grow into rod shaped nano particle as the synthesis progresses [7]. The SEM image of HA-Np (R2) showing a greater proportion of bead like particles, with an aspect ratio in the range 1.0–1.3, indicate an inhibition of the growth along the c axis. This is possible where in the synthesis procedure of HA-Np (R2), release of ammonia can hinder further growth of the crystal in c-direction leading to bead-like particles.

3.4. Quartz crystal microbalance

The stability of the deposited thin coatings was monitored using the QCM. The stability of the HA-Np coatings were investigated immediately after deposition, sonication, and prolong water exposure. The mass change at each of the above steps was measured by monitoring the change in the QCM resonance frequency. The resonance frequency of the QCM is linearly proportional to the mass accumulation or removal and is given by the Sauerbrey equation:

$$\Delta f = -\frac{2f_0^2}{A\sqrt{\mu\rho}}\Delta m$$

where f_0 is the resonance frequency of the bare QCM in air, A is the effective surface area of the electrodes, ρ and μ are the density and shear modulus, respectively of quartz [25].

The QCM resonance frequencies were monitored immediately after deposition (f_1) and after sonication in water (f_2). The sonication of the HA-Np coated QCM was carried out in steps until no net frequency shift was observed. The change in the frequency between f_0 and f_1 (i.e. $f_0 - f_1$) is proportional to the mass of HA-Np immediately after deposition. The change in the frequency f_o and f_2 (i.e. $f_0 - f_2$) is the remaining HA-Np mass on the QCM after sonication. In all data reported in this study the initial mass of HA-Np coated was in the range 1000–2000 ng. Fig. 5 shows the mass percentage of remaining HA-Np after sonication with respect to the initial mass that was deposited on the QCM electrode by EPD and spin coating techniques. It was observed that HA-Np initial mass beyond 2000 ng tend to destabilize QCM resonance frequency and therefore was not considered in this paper.

Sonication is done in order to remove loosely bound HA-Np particle from the coating surface. Sonication in a medium of interest has been extensively used for monitoring coating stabilities [9,22,39] prior to subsequent surface modifications. Further it is also a routine method used before carrying out surface analysis for coating conformation on a substrate. In general HA-Np coatings deposited using either technique showed dissolution of some amount of the initial coating during sonication, before resulting in a thin stable coating. It can be observed that the percentage amount, which is approximately 80%, of the coating remaining for HA-Np (R2) is independent of the coating technique.

In most sensor applications, it is required for these coatings to be exposed to aqueous media for varying periods of time [23,40,41]. Therefore, it is important to have coatings which are stable upon prolong exposure to aqueous media. QCM frequency measurements were taken on previously sonicated HA-Np coated samples to detect the stability of the coating after prolong exposure to water. It was observed in Fig. 6 that only the HA-Np (R2) deposited using the EPD technique show significant resistance to dissolution in water, whereas percentage remaining in all other depositions were less than 1% which indicate complete removal of the initial coating.

Calculations show that 99.5 ± 4.43% of the EPD coated HA-Np (R2), remain on the surface even after prolong exposure to water. SEM images of the above samples taken before and after prolong exposure to water is shown in Fig. 7, which further verify the existence of the coating after prolong exposure to water.

Under EPD, particles with different charge/radius ratios have different electrophoretic mobilities where smaller particles get deposited initially [21]. In EPD coated samples, Route 2 shows a higher percentage of bead like segregated particles on the surface, compared to Routes 1 and 3 that show significant particle agglomeration (See Fig. 8). As the fabrication is done under a low voltage within 3 s, the particles with smaller size initially migrate towards the surface and creates a homogeneous coating on the surface. From the particle sizes measured

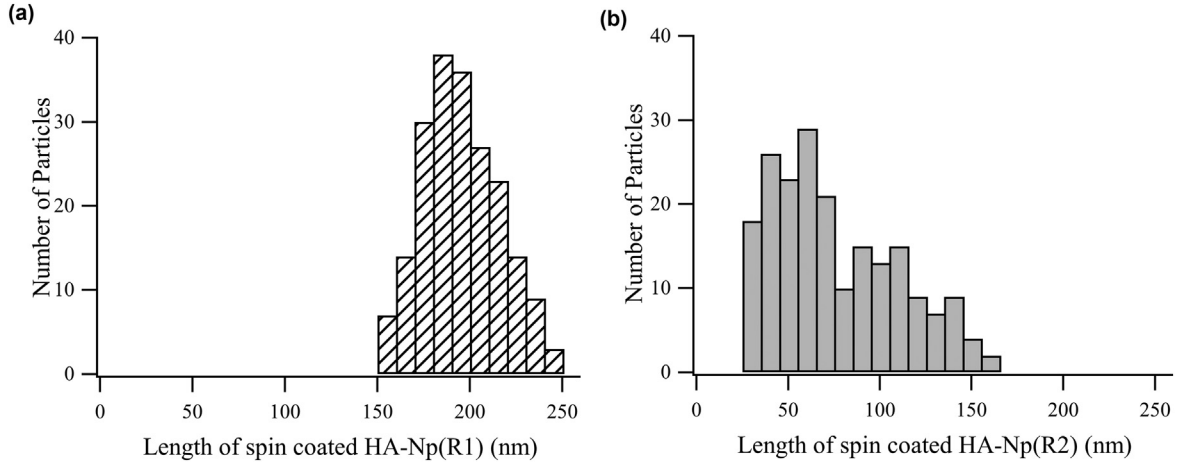

Fig. 4. Synthesized HA-Np length distribution; (a) HA-Np (R1), (b) HA-Np (R2).

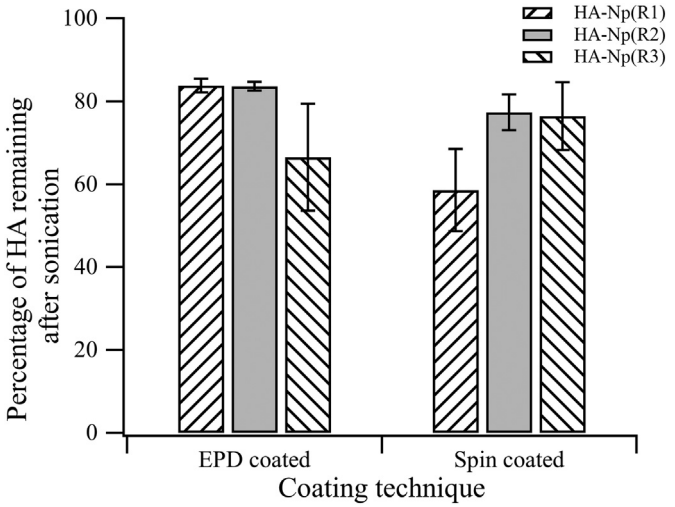

Fig. 5. Percentage of HA-Np remaining in three different routes after sonication of spin-coated & EPD-coated QCMs.

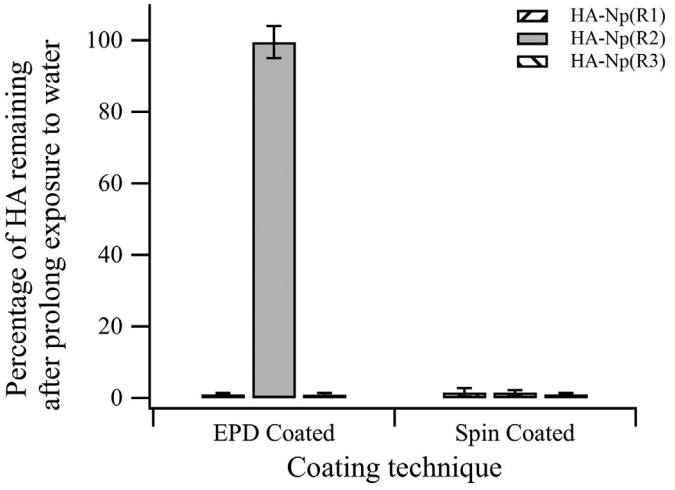

Fig. 6. Percentage of HA-Np remaining in coatings of HA-Np (R1), HA-Np (R2), and HA-Np (R3) deposited on QCM via EPD and Spin coating techniques after prolonged exposure to water.

on the HA-Np (R2) coated QCMs, shown in Fig. 3(b) and Fig. 7(a), it is evident that the size distribution of EPD coated surface show smaller particle sizes compared to that obtained on spin coated HA-Np (R2) samples. This size distribution is shown in Fig. 9(a) and 9(b).

Zhao et al., through a molecular dynamic study have reported on solid/water interfacial energies of different faces of HA. Based on their study, the negative solid/water interfacial energy ($-58.9\ mJ{\cdot}m^{-2}$) and the local hydrophobicity of the (002) plane has limited the ability of water molecules to diffuse on the (002) plane [34]. As explained previously, the growth along the *c*- axis is inhibited in HA-Np (R2) resulting in bead like particles. Thus, it is possible that the arrangement of these particles on the surface with each particle predominantly exposing (002) plane would lead to a negative solid water interfacial energy which explains the resistance of the coating towards dissolution in water. Fig. 10, is a schematic diagram that shows orientation of HA-Np arranged with (100) and (002) planes on the surface, respectively.

Zhao et al., also explained that the (100) face of HA is the most stable face, having the smallest positive solid – water interfacial energy ($324.8\ mJ{\cdot}m^{-2}$). Furthermore, it was stated that the water molecules diffuse relatively freely across the plane due to the hydrophilic nature of the entire (100) face while creating a homogeneous distribution of adsorbed water [34]. Accordingly, water molecules create a homogenous layer on the (100) plane of HA-Np coating, upon exposure to water. The porosity of the HA-Np triggers the swelling of the particles which eventually leads to the separation of each particle on the surface. Therefore, particle dissolution can occur due to hydration of the entire surface of the particle.

It is reported that there are 3 types of particle distribution structures in the Nerst layer during EPD. The particle zone close to the deposited layer can create a stable state by mutual repulsion, a flocculated state by weak attractions and a coagulated state with strong attractions [13]. Highly ordered and packed EPD coated HA-Np (R2) indicate that it is in the stable state (Fig. 7(a)). Particles synthesized by route 1 and 3 show coagulated and flocculated states, respectively. This arrangement in routes 1 and 3 can affect the (100) plane to be exposed to water and increase the dissolution. Bead-like particles preferentially arrange along c-direction to form rod-like particles [7], thus exposing greater proportion of (100) plane to water. This phenomenon could be the reason for the dissolution observed on EPD coated QCMs with HA-Np (R1), where rod-like particles are seen clustered on the surface (Fig. 8a). The dissolution observed in EPD coated HA-Np (R3) could also be related to the exposure of (100) plane as a result of particle aggregation seen on the SEM image. However, the morphology of these particles could not be resolved in the SEM image.

During spin coating, unlike in the EPD technique, particles deposit in random orientations. Therefore the loss of coating in all the samples studied after prolong exposure to water suggest that the spin coated surface would contain more of particles that are oriented with (100) plane exposed to water. This is evident in the SEM images shown in

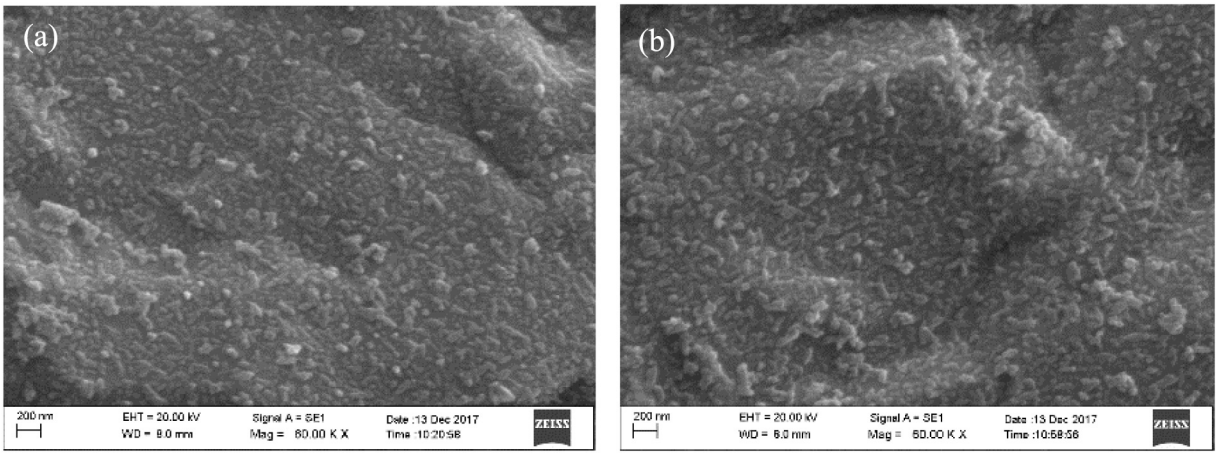

Fig. 7. SEM images of HA-Np (R2) coating deposited using EPD technique, on QCM; (a) before and (b) after prolong exposure to water. The images were taken at a magnification of 60 K X with sacle bar representing 200 nm.

Fig. 3, where rod-like particles were observed. Thus, it can be postulated that the morphology in the form of preferential crystal orientation of the HA-Np on a given surface is one of the factors that control the stability of these coatings deposited under ambient conditions.

Ionic dissolution of HA has been extensively studied [42,43]. Almost all the studies indicated that the dissolution occurs due to the degradation of HA as a result of high temperature sintering process where HA is broken down to different phases of calcium apatites in water and in acids [44–48]. On the contrary, the dissolution observed by us cannot be ascribed to a similar process as high temperature sintering was not applied to the thin HA-Np coatings.

Ex-situ measurements were carried out to monitor the ionic dissolution of HA-Np over a period of 20 h. A suspension of HA-Np powder was placed in a sealed dialysis membrane and was immersed in a beaker containing de-ionized water. It was continuously stirred at 500 rpm and the change in conductivity with time was monitored. Fig. 11 shows an increment in the conductivity of the HA-Np immersed water sample. The control (de-ionized water) does not show an increment in conductivity implying the ionic dissolution of HA-Np in water.

Rootare et al. reports that the dissolution of ions from HA creates a salting in effect [48]. Therefore, when HA-Np are immersed in water, the hydroxyl groups on HA-Np help the solvation and allow HA-Np to form hydrogen bonds with the surrounding water molecules followed by the release of ions from the surface. Moreover, it creates a charge on the HA-Np which increases the hydrophilic nature. Therefore the dissolution of HA-Np from the surface is triggered and this indicates the salting in effect in the system.

HA-Np coated QCMs were exposed to a PBS medium for a similar period of time as in water. Frequency measurements of QCMs coated with HA-Np were taken before and after exposure to PBS. Percentage of HA-Np remaining after prolong exposure to PBS is indicated in Fig. 12. Data indicates the presence of the coating. Furthermore, an increment of the weight percentage was observed by 16.6% and 19.9% in the HA-Np (R1) & HA-Np (R2) coatings, which can be related to the binding of phosphate ions to the HA-Np surface.

HA is a known ion exchanger where substitution can take place at sites where calcium, hydroxyl and phosphates occupy [37]. When the coating is immersed in water, dissolution takes place in atomic level through ion exchange. A dynamic equilibrium of phosphate ions is created due to the interchange of phosphates in the medium of the PBS with phosphates in HA-Np. As a result of the equilibrium, the dissolution is controlled in the PBS medium.

Moreover, the ion concentration is higher in the PBS medium than water. Therefore, water molecules available for the hydration of HA-Np are attracted by the ions in PBS. This eventually decreases the number of water molecules available to interact with HA-Np. Hence, as a result of the high demand for water molecules, the HA-HA interactions become stronger than water – HA-Np interactions. This finally stabilizes the coating of HA-Np as in the salting out effect. Hence, the dissolution is suppressed in the presence of PBS. This further explains that the solution at interface control the HA-Np coating stability.

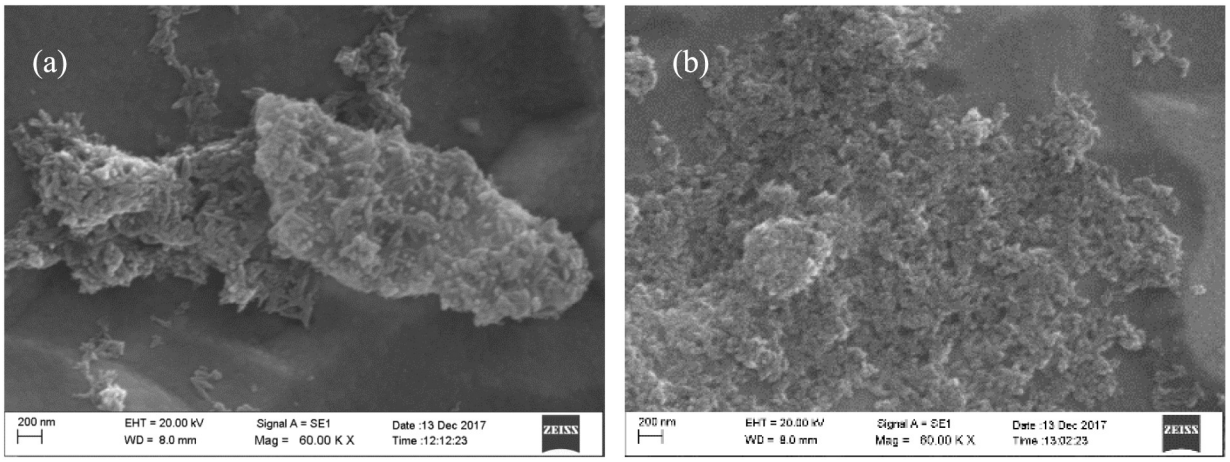

Fig. 8. SEM images of (a) HA-Np (R1) and (b) HA-Np (R3) coating deposited using EPD technique on QCM. The sacle bar represent 200 nm and image magnification 60 K X.

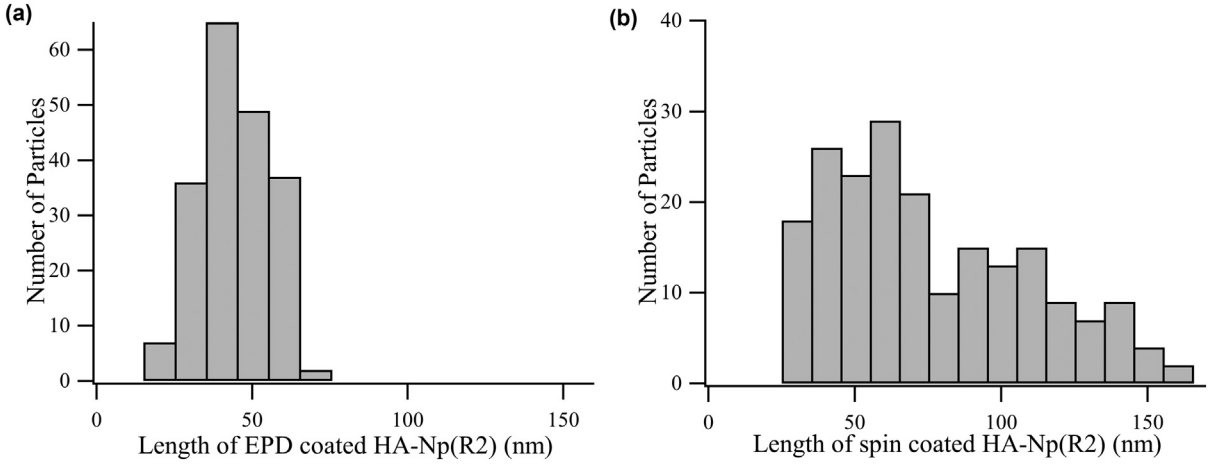

Fig. 9. EPD coated and spin coated HA-Np (R2) length distribution.

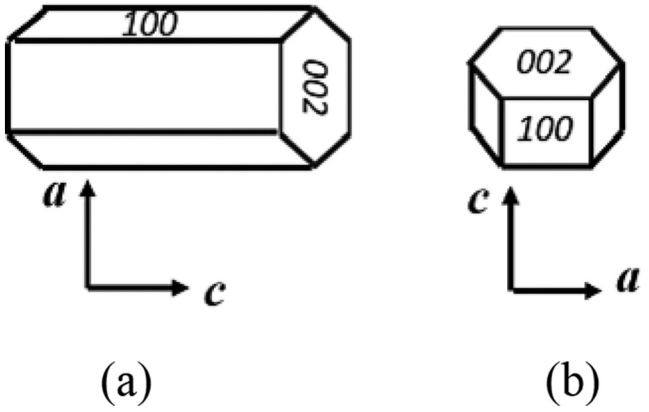

Fig. 10. Schematic illustration of the orientation of HA-Np crystal on the QCM; (a) HA-Np (R1) & HA-Np (R3) (b) HA-Np (R2).

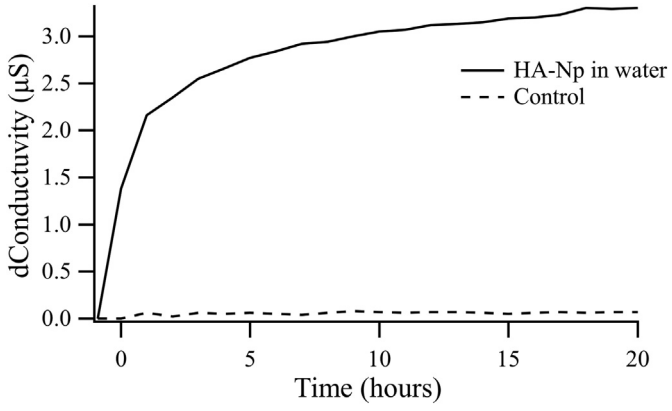

Fig. 11. Conductivity changes of HA nano-particles due to prolong exposure to water.

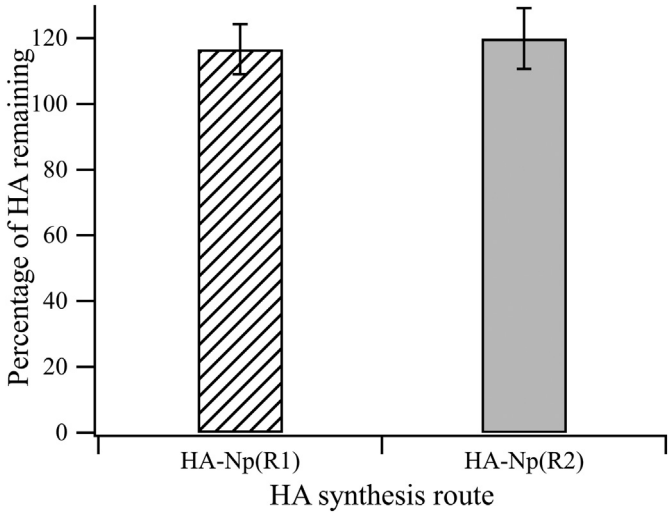

Fig. 12. Percentage of HA-Np remaining after prolong exposure to PBS.

4. Conclusion

When developing a biosensor, the stability of the fabricated material is a vital factor. HA-Np synthesized by three different routes were fabricated on QCM sensors, using EPD and spin coating techniques, without sintering at high temperatures. The resulting coatings showed quasi-stability under ultrasonic treatment in aqueous medium. The subsequent prolong exposure to water showed a stable coating on the EPD coated HA-Np (R2) and the complete removal of the rest of HA-Np coatings. HA-Np (R2) are truncated during the growth of the crystal resulting in particles with smaller size. The arrangement of these particles on the surface with each particle predominantly exposing the (002) plane would lead to a negative solid water interfacial energy which explains the resistance of the coating towards dissolution in water. Hence, the dissolution could be related to the preferential crystal orientation of the HA-Np on the gold surface. Nevertheless, all coatings showed stability in the HA-Np/PBS interface due to the salting out effect and the dynamic equilibrium created between phosphates in the solution and HA-Np. It can be concluded that the key parameters which control the stability of HA-Np coatings fabricated in ambient conditions are the surface morphology in the form of preferential crystal orientation and the solution medium at the interface.

Supplementary data to this article can be found online at https://doi.org/10.1016/j.surfcoat.2018.05.042.

Acknowledgement

Financial assistance given by the National Research Council Sri Lanka under the NRC Grant 15:04 is acknowledged. The authors would also like to acknowledge The Center for Advanced Materials Research of the University of Sri Jayewardenepura, Sri Lanka and Sri Lanka Institute of Nanotechnology for the use of their instrumentation facilities. We are also grateful to Mr. G.D.D.S. Gamage of University of Peradeniya, Sri Lanka, for his support on Scanning Electron Microscope.

References

[1] C. Elias, J.H. Lima, R. Valiev, M. Meyers, Biomedical applications of titanium and its alloys, JOM J. Miner. Met. Mater. Soc. 60 (2008) 46–49.
[2] P. Habibovic, F. Barrere, C.A. Blitterswijk, K. Groot, P. Layrolle, Biomimetic hydroxyapatite coating on metal implants, J. Am. Ceram. Soc. 85 (2002) 517–522.
[3] J.L. Ong, D.C. Chan, Hydroxyapatite and their use as coatings in dental implants: a review, Crit. Rev. Biomed. Eng. 28 (2000).
[4] D. Yu, J. Wong, Y. Matsuda, J.L. Fox, W.I. Higuchi, M. Otsuka, Self-setting hydroxyapatite cement: a novel skeletal drug-delivery system for antibiotics, J. Pharm. Sci. 81 (1992) 529–531.
[5] H.-W. Kim, J.C. Knowles, H.-E. Kim, Hydroxyapatite/poly (ε-caprolactone) composite coatings on hydroxyapatite porous bone scaffold for drug delivery, Biomaterials 25 (2004) 1279–1287.
[6] N. Kottegoda, I. Munaweera, N. Madusanka, V. Karunaratne, A green slow-release fertilizer composition based on urea-modified hydroxyapatite nanoparticles encapsulated wood, Curr. Sci. 101 (2011) 73–78.
[7] N. Kottegoda, C. Sandaruwan, G. Priyadarshana, A. Siriwardhana, U.A. Rathnayake, D.M. Berugoda Arachchige, A.R. Kumarasinghe, D. Dahanayake, V. Karunaratne, G.A. Amaratunga, Urea-hydroxyapatite Nanohybrids for slow release of nitrogen, ACS Nano 11 (2017) 1214–1221.
[8] Z. Yang, C. Zhang, Adsorption/desorption behavior of protein on nanosized hydroxyapatite coatings: a quartz crystal microbalance study, Appl. Surf. Sci. 255 (2009) 4569–4574.
[9] A. Monkawa, T. Ikoma, S. Yunoki, T. Yoshioka, J. Tanaka, D. Chakarov, B. Kasemo, Fabrication of hydroxyapatite ultra-thin layer on gold surface and its application for quartz crystal microbalance technique, Biomaterials 27 (2006) 5748–5754.
[10] K. Gross, N. Ray, M. Røkkum, The contribution of coating microstructure to degradation and particle release in hydroxyapatite coated prostheses, J. Biomed. Mater. Res. A 63 (2002) 106–114.
[11] H. Zeng, W.R. Lacefield, S. Mirov, Structural and morphological study of pulsed laser deposited calcium phosphate bioceramic coatings: influence of deposition conditions, laser parameters, and target properties, J. Biomed. Mater. Res. A 50 (2000) 248–258.
[12] A. Milev, G. Kannangara, B. Ben-Nissan, Morphological stability of hydroxyapatite precursor, Mater. Lett. 57 (2003) 1960–1965.
[13] L. Besra, M. Liu, A review on fundamentals and applications of electrophoretic deposition (EPD), Prog. Mater. Sci. 52 (2007) 1–61.
[14] P. Ducheyne, W. Van Raemdonck, J. Heughebaert, M. Heughebaert, Structural analysis of hydroxyapatite coatings on titanium, Biomaterials 7 (1986) 97–103.
[15] X. Meng, T.Y. Kwon, Y. Yang, J.L. Ong, K.H. Kim, Effects of applied voltages on hydroxyapatite coating of titanium by electrophoretic deposition, J Biomed Mater Res B Appl Biomater 78 (2006) 373–377.
[16] M. Wei, A. Ruys, M. Swain, S. Kim, B. Milthorpe, C. Sorrell, Interfacial bond strength of electrophoretically deposited hydroxyapatite coatings on metals, J. Mater. Sci. Mater. Med. 10 (1999) 401–409.
[17] X.F. Xiao, R.F. Liu, Effect of suspension stability on electrophoretic deposition of hydroxyapatite coatings, Mater. Lett. 60 (2006) 2627–2632.
[18] R. Wang, Y. Hu, Patterning hydroxyapatite biocoating by electrophoretic deposition, J. Biomed. Mater. Res. A 67 (2003) 270–275.
[19] N. Sahu, B. Parija, S. Panigrahi, Fundamental understanding and modeling of spin coating process: a review, Indian Journal of Physics 83 (2009) 493–502.
[20] Z. Yang, S. Si, C. Zhang, G. Song, Quartz crystal microbalance studies on bilirubin adsorption on self-assembled phospholipid bilayers, J. Colloid Interface Sci. 305 (2007) 1–6.
[21] I. Zhitomirsky, L. Gal-Or, Electrophoretic deposition of hydroxyapatite, J. Mater. Sci. Mater. Med. 8 (1997) 213–219.
[22] A. Monkawa, T. Ikoma, S. Yunoki, K. Ohta, M. Tanaka, Electrophoretic deposition of hydroxyapatite nanocrystal, Key Engineering Materials, Trans Tech Publ, 2006, pp. 643–646.
[23] T. Ikoma, M. Tagaya, T. Tonegawa, M. Okuda, N. Hanagata, T. Yoshioka, D. Chakarov, B. Kasemo, M. Tanaka, The surface property of hydroxyapatite: sensing with quartz crystal microbalance, Key Engineering Materials, Trans Tech Publ, 2009, pp. 89–92.
[24] I. Ben-Dov, I. Willner, E. Zisman, Piezoelectric immunosensors for urine specimens of chlamydia trachomatis employing quartz crystal microbalance microgravimetric analyses, Anal. Chem. 69 (1997) 3506–3512.
[25] D.A. Buttry, Applications of the quartz crystal microbalance to electrochemistry, Wyoming Univ Laramie Dept Of Chemistry, 1989.
[26] F. Caruso, E. Rodda, D.N. Furlong, K. Niikura, Y. Okahata, Quartz crystal microbalance study of DNA immobilization and hybridization for nucleic acid sensor development, Anal. Chem. 69 (1997) 2043–2049.
[27] C. Kößlinger, S. Drost, F. Aberl, H. Wolf, S. Koch, P. Woias, A quartz crystal biosensor for measurement in liquids, Biosens. Bioelectron. 7 (1992) 397–404.
[28] J. Langford, K. Pavey, C. Olliff, P. Cragg, G. Hanlon, F. Paul, G. Rees, Real-time monitoring of stain formation and removal on calcium hydroxyapatite surfaces using quartz crystal sensor technology, Analyst 127 (2002) 360–367.
[29] A.Y. Pataquiva Mateus, M. Ferraz, F. Monteiro, Microspheres based on hydroxyapatite nanoparticles aggregates for bone regeneration, Key Engineering Materials, Trans Tech Publ, 2007, pp. 243–246.
[30] M.H. Santos, M.D. Oliveira, L.P.D.F. Souza, H.S. Mansur, W.L. Vasconcelos, Synthesis control and characterization of hydroxyapatite prepared by wet precipitation process, Mater. Res. 7 (2004) 625–630.
[31] M. Wei, A. Ruys, B. Milthorpe, C. Sorrell, Precipitation of hydroxyapatite nanoparticles: effects of precipitation method on electrophoretic deposition, J. Mater. Sci. Mater. Med. 16 (2005) 319–324.
[32] K.-Y. Kwon, E. Wang, M. Nofal, S.-W. Lee, Microscopic study of hydroxyapatite dissolution as affected by fluoride ions, Langmuir 27 (2011) 5335–5339.
[33] D. Aquilano, M. Bruno, M. Rubbo, F.R. Massaro, L. Pastero, Low symmetry polymorph of hydroxyapatite. Theoretical equilibrium morphology of the monoclinic Ca5 (OH)(PO_4) 3, Cryst. Growth Des. 14 (2014) 2846–2852.
[34] W. Zhao, Z. Xu, Y. Yang, N. Sahai, Surface energetics of the hydroxyapatite nanocrystal–water interface: a molecular dynamics study, Langmuir 30 (2014) 13283–13292.
[35] D.R. Jayasundara, R.J. Cullen, L. Soldi, P.E. Colavita, In situ studies of the adsorption kinetics of 4-nitrobenzenediazonium salt on gold, Langmuir 27 (2011) 13029–13036.
[36] Z. Jian, W. Hejing, The physical meanings of 5 basic parameters for an X-ray diffraction peak and their application, Chin. J. Geochem. 22 (2003) 38–44.
[37] H. Wang, L. Yuan, J. An, Crystallographic characteristics of hydroxylapatite in hard tissues of *Cololabis saira*, Crystals 7 (2017) 103.
[38] D. Lin-Vien, N.B. Colthup, W.G. Fateley, J.G. Grasselli, The Handbook of Infrared and Raman Characteristic Frequencies of Organic Molecules, Elsevier, 1991.
[39] O. Abramov, A. Gedanken, Y. Koltypin, N. Perkas, I. Perelshtein, E. Joyce, T. Mason, Pilot scale sonochemical coating of nanoparticles onto textiles to produce biocidal fabrics, Surf. Coat. Technol. 204 (2009) 718–722.
[40] S. Si, L. Si, F. Ren, D. Zhu, Y. Fung, Study of adsorption behavior of bilirubin on human-albumin monolayer using a quartz crystal microbalance, J. Colloid Interface Sci. 253 (2002) 47–52.
[41] P.E. Sheehan, L.J. Whitman, Detection limits for nanoscale biosensors, Nano Lett. 5 (2005) 803–807.
[42] E. Mavropoulos, A.M. Rossi, N.C. da Rocha, G.A. Soares, J.C. Moreira, G.T. Moure, Dissolution of calcium-deficient hydroxyapatite synthesized at different conditions, Mater. Charact. 50 (2003) 203–207.
[43] H.-G. Linge, Dissolution of ionic crystal surfaces, Adv. Colloid Interf. Sci. 14 (1981) 239–250.
[44] Z.-F. Chen, B. Darvell, V.-H. Leung, Hydroxyapatite solubility in simple inorganic solutions, Arch. Oral Biol. 49 (2004) 359–367.
[45] H. Kaufman, I. Kleinberg, Studies on the incongruent solubility of hydroxyapatite, Calcif. Tissue Int. 27 (1979) 143.
[46] P. Gramain, J. Thomann, M. Gumpper, J. Voegel, Dissolution kinetics of human enamel powder: I. Stirring effects and surface calcium accumulation, J. Colloid Interface Sci. 128 (1989) 370–381.
[47] F. Fazan, P.M. Marquis, Dissolution behavior of plasma-sprayed hydroxyapatite coatings, J. Mater. Sci. Mater. Med. 11 (2000) 787–792.
[48] H.M. Rootare, V.R. Deitz, F.G. Carpenter, Solubility product phenomena in hydroxyapatite-water systems, J. Colloid Sci. 17 (1962) 179–206.